RESEARCH PAPER

Stream of droplets as an actuator for oscillatory flows in microfluidics

Pedro Andrés Basilio[1] · Aimee M. Torres Rojas[2] · Eugenia Corvera Poiré[2,3] · Luis F. Olguín[1]

Abstract

Oscillatory or pulsatile flow in microfluidic devices is usually imposed and controlled by external electronic or mechanical actuators, limiting the chips' portability and increasing the complexity of their control. Here, we have developed a microfluidic platform that generates an oscillatory motion in a fluid with zero-mean flow, using a continuous stream of droplets as the pulsatile power source. The passage of each droplet produces an oscillatory flow in an orthogonal channel that we use to periodically force an interface between two non-miscible fluids. A detailed analysis of the dynamics of the pulsatile fluid interface revealed that its dynamics is dominated by a single oscillatory mode with precisely the same frequency of the passing droplets. As the droplets were formed by syringe-pump-driven flows of water and oil and because their frequency production can be easily controlled, it was possible to impose specific oscillatory frequencies to the fluid interface. By studying the interface movement, we propose a simple way to estimate the pressure drop caused by the flow of each droplet. This work represents a new way to produce pulsatile flow employing only continuous flows and it is an example of a microfluidic functional device that requires minimal external equipment for functioning.

Keywords Pulsatile flow · Droplet pressure drop · Microfluidic actuation · Microfluidic droplets · Oscillatory motion · Interface dynamics

1 Introduction

Oscillatory or pulsatile flow in microfluidics is normally referred to a fluid movement in which the flow direction changes cyclically back and forth, giving a zero-mean net mass transfer over each cycle. In microfluidics, oscillatory flow (also known as reciprocating flow) has found many applications. It has been employed to increase the efficiency of liquid–liquid extraction of organic compounds (Xie et al. 2015; Lestari et al. 2016), promote the mixture of parallel water streams (Tabeling et al. 2004; Wang et al. 2011), align anisotropic particles (Alizadehgiashi et al. 2018), study DNA elongation (Jo et al. 2009) and carry out chemical reactions in multiphase flow (Abolhasani and Jensen 2016). Oscillatory flows are also being studied as cooling agents in micro-scale heat transfer devices for modern electronics and photonic systems (Qu et al. 2017).

There are different strategies for imposing oscillatory flows in microchannels. The most common is the use of programmable syringe pumps with infusion/withdrawal capabilities (Jo et al. 2009; Lestari et al. 2016; Alizadehgiashi et al. 2018). It is also possible to apply alternating pressure gradients at the two ends of a channel employing electromagnetic valves (Abolhasani and Jensen 2016). Other options are to work with piezoelectric actuators to impose distinct ranges of oscillating frequencies to the fluids (Xie et al. 2015; Vázquez-Vergara et al. 2017), the use of air bubbles controlled by a high-resolution stepper-motor (Khoshmanesh et al. 2015) or by microheaters (Wang et al. 2011), and the use of electroosmotic pumps (Bengtsson et al. 2018).

✉ Eugenia Corvera Poiré
eugenia.corvera@gmail.com

✉ Luis F. Olguín
olguin.lf@comunidad.unam.mx

[1] Laboratorio de Biofisicoquímica, Facultad de Química, Universidad Nacional Autónoma de México, 04510 Ciudad de México, Mexico

[2] Departamento de Física y Química Teórica, Facultad de Química, Universidad Nacional Autónoma de México, 04510 Ciudad de México, Mexico

[3] Imaging Sciences and Biomedical Engineering Division, St Thomas Hospital, Kings College, London, UK

In all the previous examples, the fluid oscillation inside the device requires external apparatus and electronics for actuation. This reduces the portability of the microchips and increases the operation cost. Having microfluidic devices with a minimum or without external mechanical or electronic actuators is the aim of an increasing number of research papers looking for independent devices capable of performing complex operations in flow delivery and control (Leslie et al. 2009; Mosadegh et al. 2010; Duncan et al. 2013; Kim et al. 2015, 2018; Zhang et al. 2017; Wang et al. 2018).

Here, we designed and characterized a simple microfluidic chip that evades the use of piezoelectrics, valves or other mechanical motors to generate pulsatile fluid motion with zero-mean flow in microfluidic devices. Our chip employs a moving train of droplets to generate a pulsatile driving pressure that can be used, in turn, to pulsate a fluid–fluid interface in a perpendicular channel. The droplets were formed by continuous syringe-pump-driven flows of water and oil and, because their frequency production and size can be significantly controlled (Garstecki et al. 2006; Jose and Cubaud 2014; Lignel et al. 2017), it was possible to impose specific oscillatory frequencies to the fluid interface. We characterized the dynamics of the periodic interfacial movement by following the position of the liquid–liquid interface and found that a single oscillatory mode correlates precisely with the droplet frequency, demonstrating the possibility of imposing an oscillatory forcing solely with hydrodynamic elements. Also, by studying the interface movement we propose a simple way to estimate the pressure drop caused by the flow of each droplet. Finally, we discuss briefly possible applications for our microfluidic device.

2 Experimental design

2.1 Design and operation principles of the microfluidic device

A flow-focusing design was chosen to generate water-in-oil microdroplets that traveled through a straight 9.0-mm-long channel until its exit (Fig. 1, panels 1, 2). A perpendicular channel, partially filled with oil and an oil-immiscible fluid (water in this work), intersects the droplet channel at half its length forming a T-junction. In this perpendicular channel, the liquid–liquid interface, whose dynamics will be studied, is near the T-junction (Fig. 1, panel 3).

The pressure along the microfluidic channel transporting the water droplets does not follow a simple linear decay (corresponding to a single-phase flow with a constant gradient), but it has discrete steps imposed over the linear decay due to the droplet's presence (Baroud et al. 2010). Each time a droplet passes by the T-junction, it generates a pulsatile pressure that
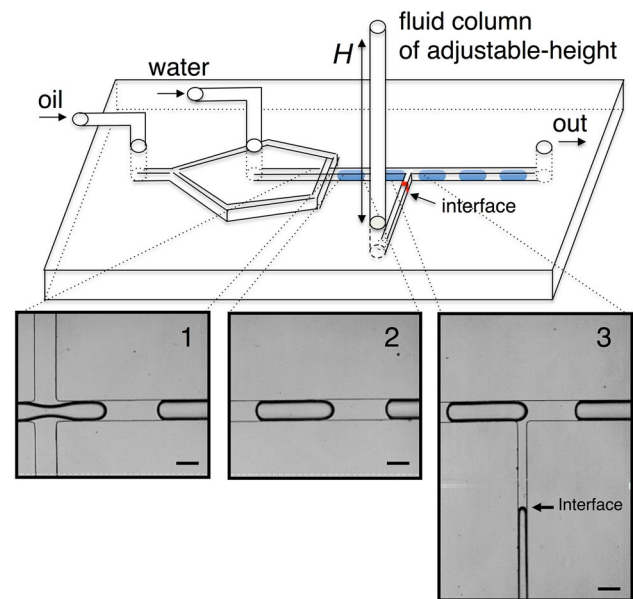

Fig. 1 Above: Schematic diagram of the microfluidic device made from polydimethylsiloxane (PDMS). Below: Panel 1: Optical microscope image showing the water droplet formation at the flow-focusing configuration. Panel 2: Optical microscope image of droplets traveling through the channel. Panel 3: Optical microscope image of the perpendicular channel with a fluid–fluid interface. Scale bar: 175 μm

is transduced in an observable oscillatory movement of the interface. The droplet frequency can be fine-tuned by modifying the water and oil flow rates, giving the opportunity to impose different forcing frequencies to the interface. To keep the interface oscillating roughly at the same average position for each frequency, the inlet of the perpendicular channel was connected to a fluid column of adjustable height (Fig. 1). The hydrostatic pressure imposed by this liquid column compensates the fluid pressure at the T-junction to have the same average pressure at both sides of the interface channel.

Figure 2 shows the experimental fluid pressure at the base of the liquid column, ΔP, at various total flow rates, Q_t, in the droplet microchannel (black squares). The total flow rate, Q_t, is the sum of oil and water flows ($Q_t = Q_o + Q_w$) and the fluid pressure was calculated as

$$\Delta P = \rho \cdot g \cdot H, \tag{1}$$

where ρ is the water density, g the acceleration of gravity and H the height of the liquid column relative to the microchannel.

Also, in Fig. 2 we present, for reference, the pressure drop calculated for a single-phase laminar flow of mineral oil at the T-junction as a function of total flow:

$$\Delta P = Q_t \cdot R_H, \tag{2}$$

where R_H is the hydraulic resistance, which was calculated considering two different geometries of the cross-sectional
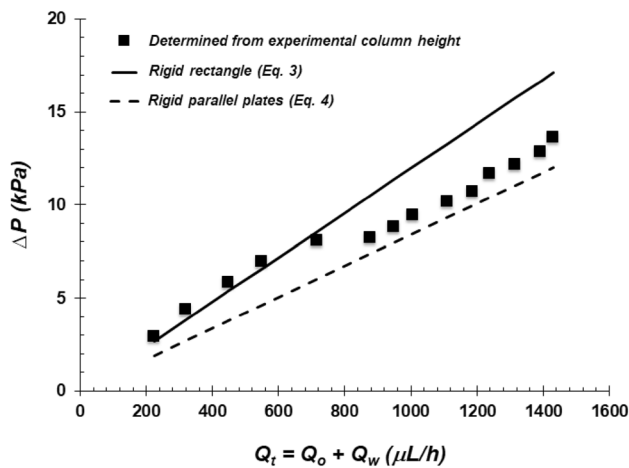
Fig. 2 Pressure of water at the perpendicular microchannel determined from the height of the fluid column (Eq. 1) against the total flow (oil + water) in the microchannel containing the droplets (black squares). Calculated pressure drop of a single-phase flow of mineral oil (continuous phase) in a rectangular cross-sectional microchannel using Eqs. (2) and (3) (solid line) or with a parallel plate model using Eqs. (2) and (4) (dashed line)

area of the channel. The first one (Eq. 3) is for a fluid in a rigid channel with a rectangular cross-sectional area of width, W, larger than its height, h ($W > h$) (Bruus 2008):

$$R_H = \left(\frac{12\eta D}{h^3 W} \right) \left(\frac{1}{1 - 0.63(h/W)} \right), \tag{3}$$

where D is the distance from the flow-focusing point to the T-junction ($D = 4.5$ mm) and η is the dynamic viscosity of the mineral oil employed ($\eta = 56$ mPa s).

The second hydraulic resistance is for a fluid between two rigid parallel plates, valid when $W >> h$ (Bruus 2008):

$$R_H = \left(\frac{12\eta D}{h^3 W} \right). \tag{4}$$

Figure 2 shows that at low flow rates, the experimental pressure approximates well to the one calculated with R_H for a rectangular cross-sectional area ($W > h$). This is expected because the microchannel used in the experiments has an aspect ratio $W/h = 2.1$. However, at high flow rates, the experimental pressure deviates from this model and lies above the parallel plate prediction. The same qualitative results have been obtained in experiments of pressure drop as a function of flow rate in rectangular PDMS channels with W/h ratios of 2.1 (Cheung et al. 2012). These findings were well explained based on the deformation of the elastic PDMS walls at higher flow rates. Experimentally, the deflection of PDMS channels has been verified and measured by different research groups with distinct techniques (see for example: Kang et al. 2014; Raj and Sen 2016).

Although there are different analytical models to describe the pressure drop caused by a train of droplets in a microchannel (Bordbar et al. 2018; Ładosz and von Rohr 2018), it was difficult to make a good fit between our experimental data and the predicted values (see Online Resource 1). This is because the models are optimized for very specific channel geometries and flow regimes, which limits their agreement with experimental values.

Based on the pressure result obtained from the liquid column at different flow rates, we consider that they reflect with a good approximation the average pressure at the T-junction (at the opposite extreme of the interface channel). Though, to account for the pressure jump caused by the pass of each droplet it is necessary to measure the interface movement as explained in Sects. 2.3 and 3.2.

2.2 Droplet characterization

We produced water-in-oil droplets at different flow rates of oil (Q_o) and water (Q_w), maintaining the flow ratio equal to one ($Q_o/Q_w = 1$) in all the experiments. Under this condition, the droplet capillary number Ca $= \eta \cdot V/\gamma$ (where η is the dynamic viscosity of the mineral oil, V is the droplet velocity and γ is the interfacial tension between water and oil-containing surfactant) increased linearly with the total flow $Q_t = Q_o + Q_w$ (Fig. 3a). The droplet angular frequency, ω_d, calculated from the number of droplets passing close to the T-junction per unit time as $\omega_d = 2\pi/T$, where T is the average time between droplets, also follows a linear increase with total flow (Fig. 3b), demonstrating a simple way to change the pulsatile forcing frequency over the interface.

Figure 4 shows the reduction of three characteristic lengths of the droplets as the capillary number Ca increases. Figure 4a shows the droplet width, w. We can see that when Ca < 0.3, the droplet width occupies almost the whole channel leaving only a thin lubrication film of oil between the microfluidic droplets and the PDMS walls (Chen et al. 2015; Bordbar et al. 2018). As Ca increases, the droplet width diminishes and the oil lubrication film becomes thicker (it is actually visible). The droplet length, L, and the distance between droplets, d, are shown in Fig. 4b, c, respectively. Both quantities decrease monotonically with Ca, resulting in an increment in the total number of droplets in the channel from seven to twelve (three to six in the first half of the channel before the T-junction). Droplet size reduction as Ca increases has been well documented in the literature (Vanapalli et al. 2009; Sajeesh et al. 2014; Jakiela 2016) and can potentially modify the hydrodynamic resistance of droplets and affect the pulsatile pressure in the T-junction. To consider this potential change, we calculated the ratio between droplet length, L, and droplet width, w, (L/w), as it is one

Fig. 3 **a** Droplet capillary number as a function of total flow. A power regression of the data indicates that $Ca \sim Q_t^{1.02}$. **b** Droplet frequency as a function of total flow. A power regression of the data indicates that droplet frequency is almost linear with Q_t, i.e., $\omega_d \sim Q_t^{1.18}$
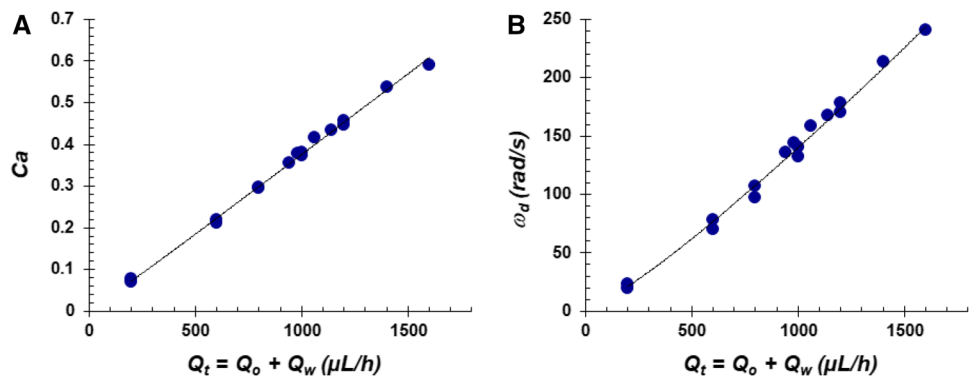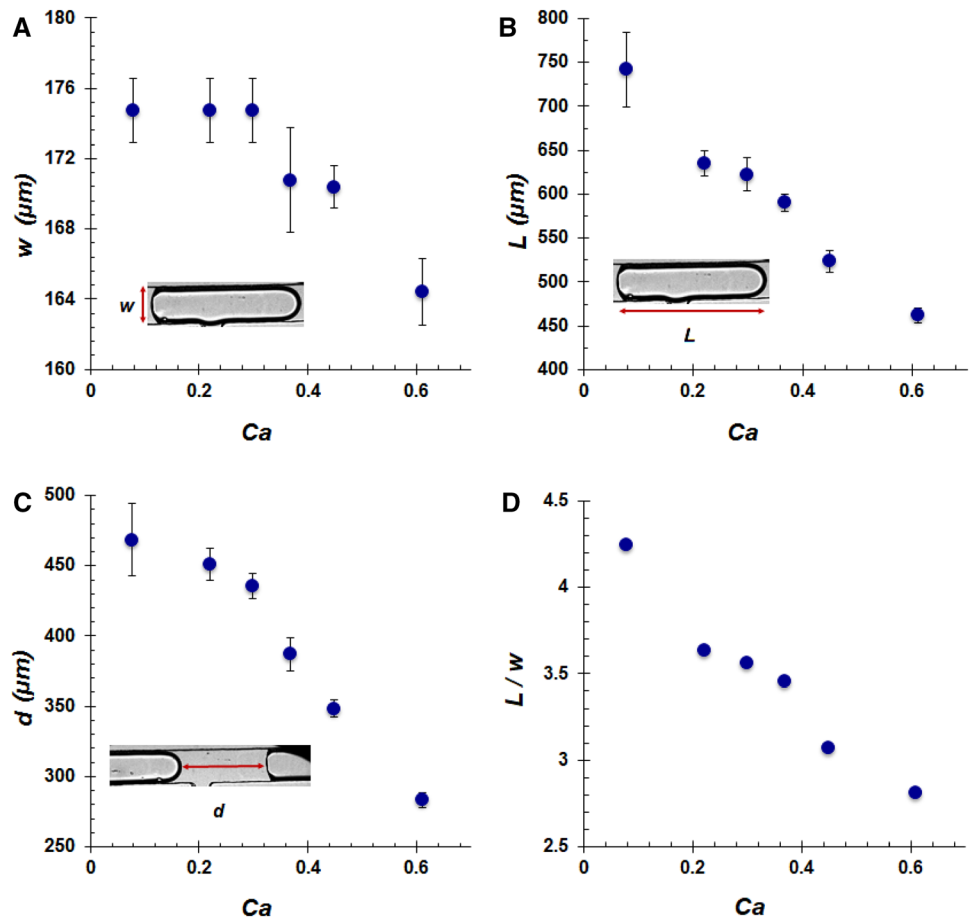

Fig. 4 Droplet characteristic sizes as a function of capillary number. **a** Droplet width, w, vs. Ca. **b** Droplet length, L, vs. Ca. **c** Distance between droplets, d, vs. Ca. **d** Droplet length/droplet width (L/w), vs. Ca

of the most important parameters for the hydrodynamic droplet resistance (Vanapalli et al. 2009; Sajeesh et al. 2014; Jakiela 2016). For the interval of capillary number studied here, the (L/w) of the droplets changed from 4.3 to 2.7 (see Fig. 4d). In this range of L/w ratios, the hydraulic resistance of the droplets is at its maximum and does not change considerably (~ 10%) (Vanapalli et al. 2009; Jakiela 2016). This suggests that each of the passing droplets will cause pressure fluctuations of approximately the same magnitude in the range of flows studied.

2.3 Interface characterization

By performing a detailed image analysis of the droplets crossing the T-junction together with the interface movement, we determined that each passing droplet generates one cycle of oscillatory movement of the interface (Fig. 5). We also noted that, in general, the lowest position of the interface (farthest from the T-junction) during an oscillation was observed when the oil plug between two droplets was crossing the T-junction. Meanwhile, the highest position of the interface (closest to the T-junction) in a cycle was recorded
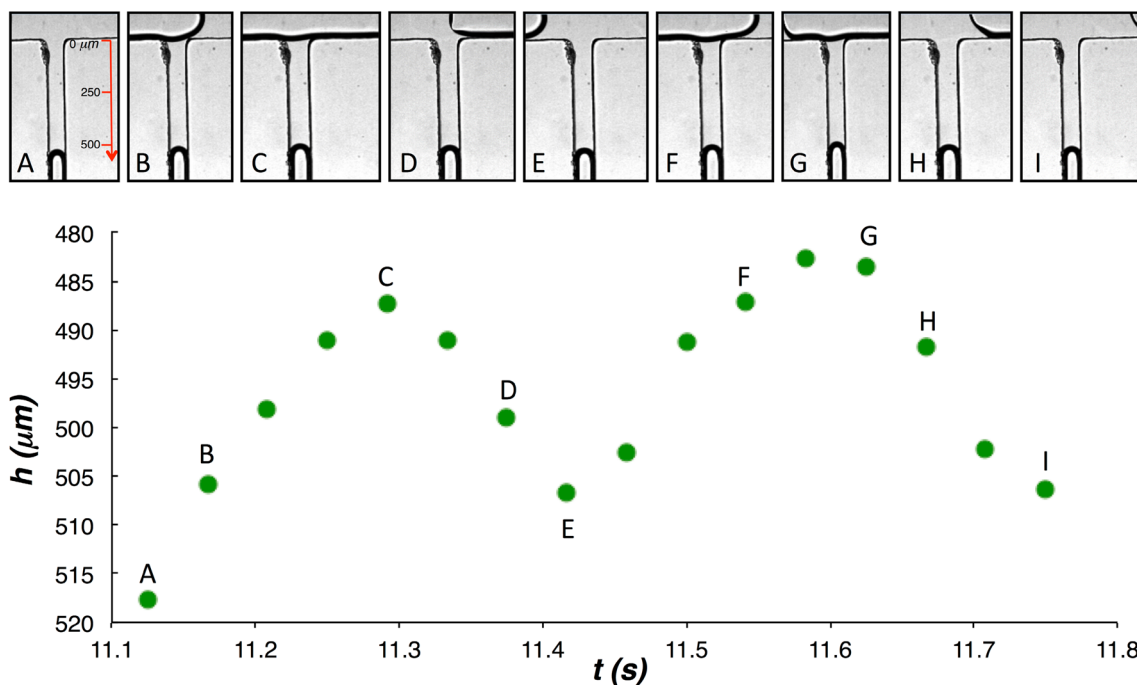
Fig. 5 **a–i** Sequential images of two droplets crossing the T-junction ($Q_t = 200$ µL/h; $\omega_d = 20.3$ rad/s). The lowest position of the interface was recorded when a plug of oil between two droplets was crossing the T-junction (**a**, **e**, **i**). Below it is shown the position of the interface as a function of time for two cycles. The T-junction was arbitrarily used as the origin

when roughly between half and two-thirds of each droplet had crossed the T-junction.

An example of the raw data of the interface position as a function of time, $h(t)$, after many droplets have traveled through the upper channel is shown in blue in Fig. 6a. The position of the interface was obtained from video image analysis and the T-junction was arbitrarily used as the origin. The interface oscillates with the passage of droplets, while having a net displacement that moves it closer or away from the T-junction at different times. It is likely that this displacement has its origin in the step motors of the syringe pumps employed, which have low-frequency flow fluctuations (Kalantarifard et al. 2018). Another probable source of fluctuations could be related to the small deformations of the PDMS channel walls—giving a wavelength of the order of the channel length—induced by the flow (Raj and Sen 2016). As we were interested on the interface movement imposed by the microdroplets, we subtracted the low-frequency trend (pink line in Fig. 6a) from the raw data and obtained the dynamics of the interface position as a function of time, $h^*(t)$, (Fig. 6b). Fourier transform of the data allowed us to obtain the interface position in frequency domain, $\hat{h}^*(\omega)$ (shown in Fig. 6c). The signal obtained in Fourier domain is typical of a dynamics dominated by a single Fourier mode that includes its harmonics. The frequency of the main peak indicates the dominant mode of oscillation of the interface, and from now on in the manuscript it is denoted as ω_i. Also,

the peak height in Fig. 6c corresponds to half the amplitude of the interface oscillation. Figure 6d shows the interface frequency vs. the droplet frequency, as well as a straight line with slope, $m = 1$. The results mean that the interface and droplet frequencies correlate very closely and that the interface is following the dynamics imposed by the stream of droplets. In more general terms, we could say that the stream of droplets imposes the pulsatile driving force that determines the interface dynamics.

3 Results and discussion

3.1 Interface dynamics

In Fig. 7a, we show the time average of the interface position, $\langle h(t) \rangle_t$, for each of the dominant frequencies of the interface. We observe that the average position of the interface in the microchannel is basically independent of its oscillation frequency. By doing a numerical derivative point by point of the $h(t)$ raw data, we obtained the instantaneous velocity of the interface, v, as a function of time. An example of the data is depicted in Fig. 7b, which was built from the raw data presented in blue in Fig. 6a. In Fig. 7c, we show the time average of the velocity, $\langle v(t) \rangle_t$, for each interface frequency. These average values are scattered around zero. Positive and negative

Fig. 6 **a** Raw data of the interface position as a function of time (blue points). Also shown is the low-frequency trend (pink line). **b** Interface position as a function of time after subtracting the low-frequency trend. **c** Fourier transform of the data shown in **b**. **d** The frequency of the interface oscillation (ω_i) computed by Fourier analysis versus the droplet driving frequency (ω_d), which was measured by counting the number of droplets per unit time, shows that the interface follows the dynamics imposed by the stream of droplets. A line with slope $m = 1$ is shown for reference
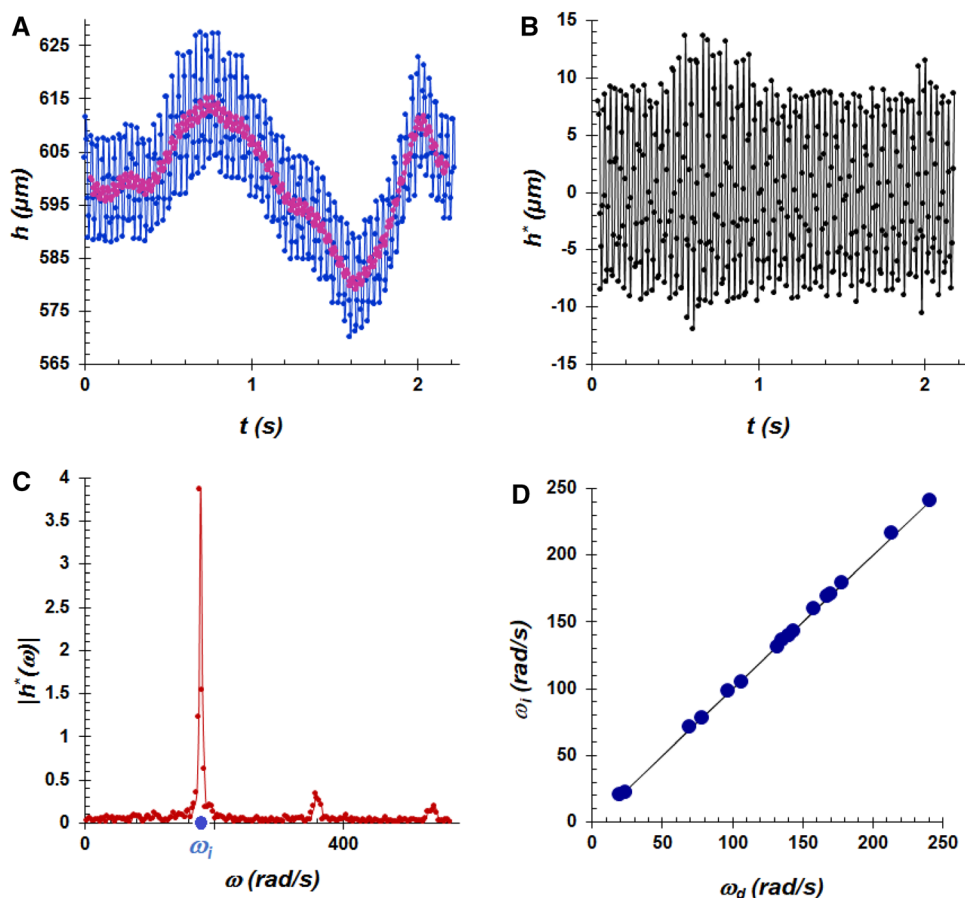
values indicate that the global displacement of the interface is toward the T-junction or away from it, respectively. However, no global tendency as a function of frequency is observed.

To isolate the movement of the interface caused only by the droplet passage, we calculated the interface velocity $v^*(t)$ using the interface position data after removing the global displacement $h^*(t)$ (see Fig. 6b). In Fig. 8a, we present $v^*(t)$ for three different frequencies, showing that the dispersion of velocities increases with frequency. We considered the standard deviation of the velocity data, σ_{v^*}, as an approximated value of the amplitude of the velocity for each frequency. These results are shown in Fig. 8b, where it can be observed that the amplitude of the velocity increases as a function of frequency. A power regression of the data shows that $\sigma_{v^*} \sim \omega_i^{0.58}$ (Fig. 8b). The average velocity values $\langle v^*(t) \rangle_t$ for each frequency are scattered around zero (Fig. 8c) as those obtained with the raw data (Fig. 7c). However, the values here are much smaller because the global displacement has been removed.

In Fig. 9a, we show the amplitude of the dominant mode of the interface position as a function of frequency. This one was obtained from the peak of the interface position in frequency domain, as explained in Sect. 2.3. We can observe that the overall tendency is a slight reduction of the oscillation amplitude with frequency.

A characteristic velocity of the interface could be obtained by multiplying the amplitude of the dominant mode by its frequency: $v_{charact} =$ amplitude $* \omega_i$. Figure 9b shows this characteristic velocity as a function of frequency. The visual similarity with data from Fig. 8b is clear.

To estimate how close the interface movement is to the dynamics of a single mode, we plot the ratio $v_{charact}/\sigma_{v^*}$ in Fig. 10. A ratio close to one indicates that the interface dynamics has basically one Fourier mode, while a ratio different from one indicates that the interface has a more complex dynamics. We can see that despite the scattering of the data around a value of one, there is basically no tendency as a function of frequency.

3.2 Pressure drop of moving droplets

An interesting feature of our device is that it is possible to estimate variations of pressure due to the pass of a single moving droplet employing our acquired interface velocity data. For low-frequency movements, we can write the relation between pressure drop in the interface microchannel and velocity as
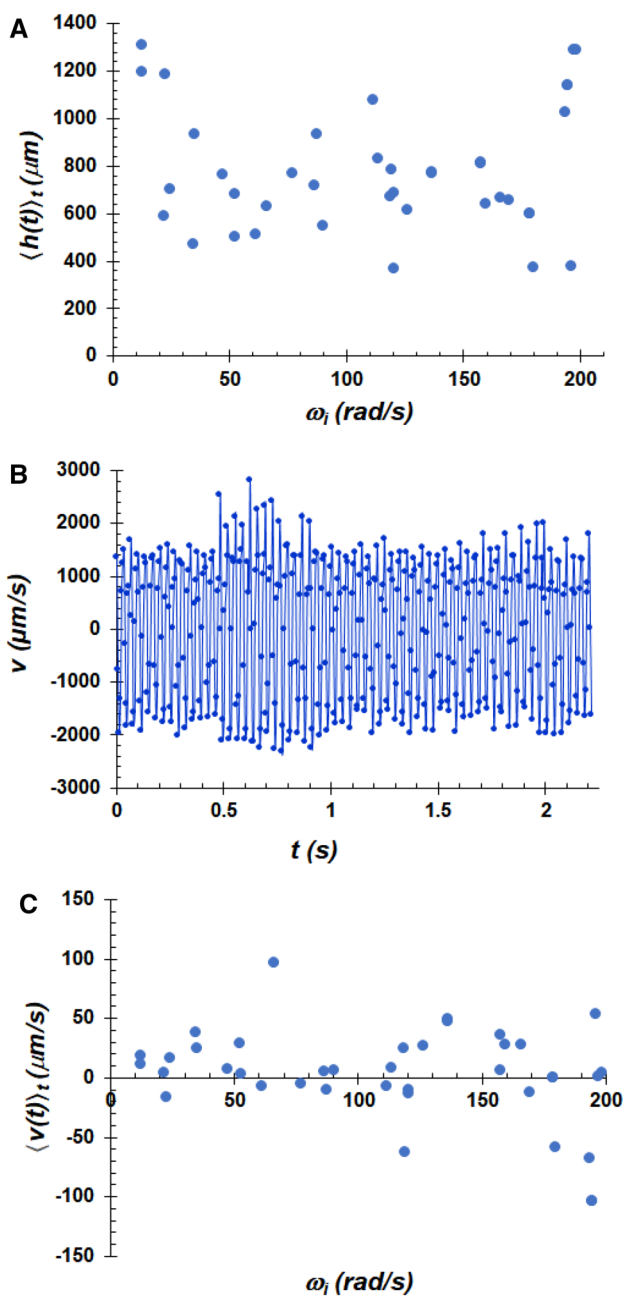
Fig. 7 a Time average of the interface position in the microchannel, $\langle h(t) \rangle_t$, as a function of the interface frequency, ω_i. **b** Interface velocity as a function of time from the raw data presented in blue in Fig. 6a. **c** Time average of the interface velocity, $\langle v(t) \rangle_t$, as a function of the interface frequency, ω_i

Fig. 8 a $v^*(t)$ for three driving frequencies: 50 rad/s in yellow, 170 rad/s in red and 180 rad/s in black. **b** Standard deviation of the velocity data, σ_{v^*}, as an approximated value of the amplitude of the velocity, as a function of the interface frequency, ω_i. A power regression of the data indicates that $\sigma_{v^*} \sim \omega_i^{0.58}$. **c** Time average velocity values, $\langle v^*(t) \rangle_t$, for each of the driving frequencies, ω_i

$$\Delta P(t) = v(t) \cdot A \cdot R_H, \tag{5}$$

where $v(t)$ is the instantaneous velocity of the interface, A is the cross-sectional area of the interface channel and R_H its hydraulic resistance. In this way, variations in pressure are linearly related to variations in velocity. To compute the hydraulic resistance (Eq. 3), we use the dimensions of the
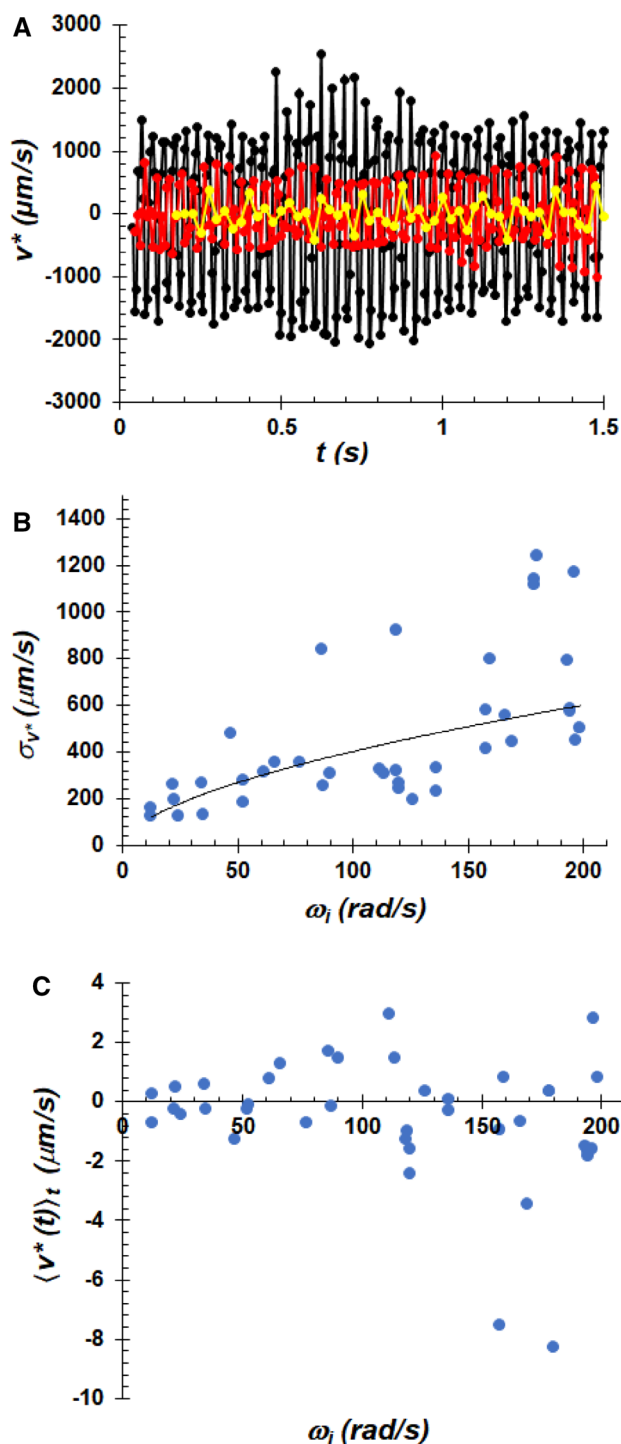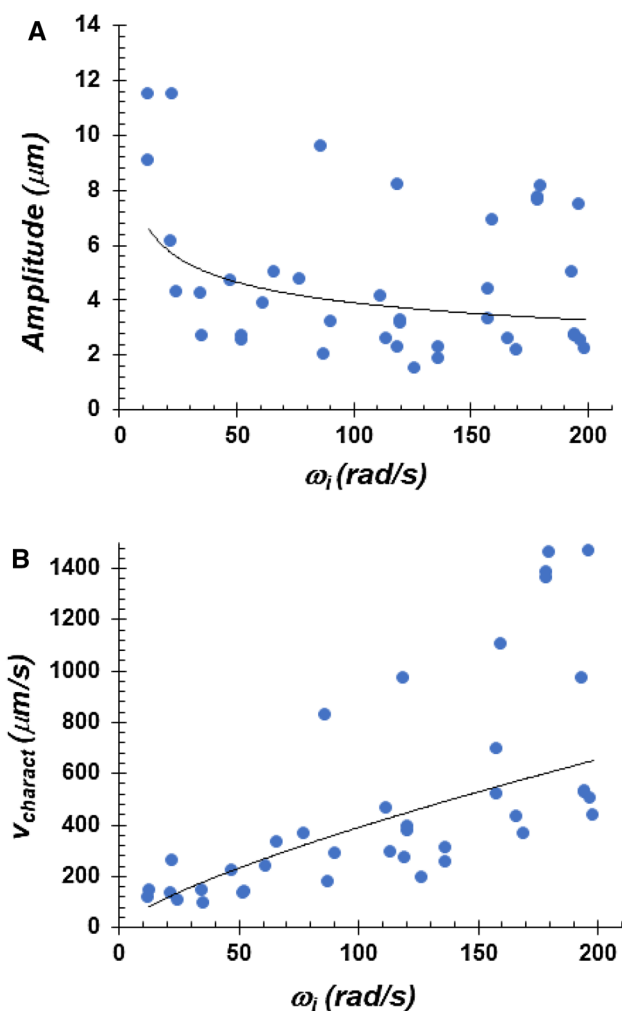
Fig. 9 **a** Amplitude of the dominant mode of the interface position as a function of frequency, ω_i. A power regression of the data indicates that the amplitude $\sim \omega_i^{-0.25}$. **b** Characteristic velocity of the interface, calculated as $v_{charact} = \text{Amplitude} * \omega_i$ for each of the frequencies, ω_i. A power regression of the data indicates that $v_{charact} \sim \omega_i^{0.75}$
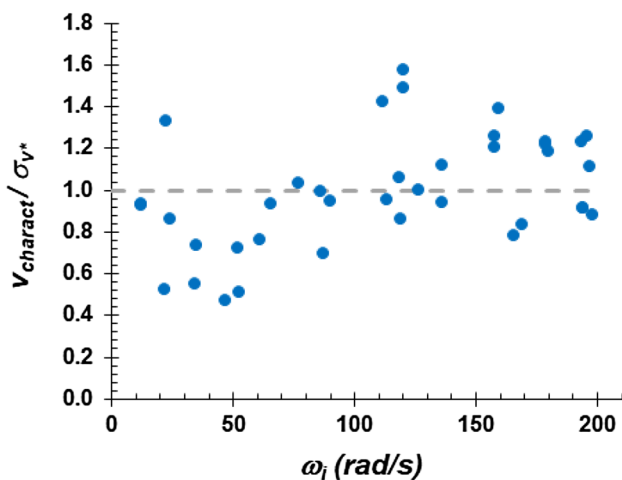

Fig. 10 Ratio $v_{charact}/\sigma_{v^*}$ as a function of frequency

interface channel and an effective viscosity for the fluids inside this channel defined as

$$\eta_{\text{eff}} = \chi_{H_2O}\eta_{H_2O} + \chi_{\text{oil}}\eta_{\text{oil}},$$

where χ_{H_2O} and χ_{oil} are the volumetric fractions that water and oil occupy in the channel, respectively. Using the data presented in Figs. 7a and 8b as well as Eqs. (3) and (5), we calculated variations of pressure at the interface channel generated by the passing of droplets and found values in the range (40–350) Pas. Because the interface channel and the channel with droplets have different dimensions (the width of the interface channel is 0.42-fold the width of the droplet channel), the variation in the pressure caused by the passage of a droplet in each of these channels is different. From Eq. (2) written for each of the channels and equating the flow caused by the passage of a single droplet in them, the following relationship is obtained:

$$\Delta P_1 = \frac{R_{H1}}{R_{H2}}\Delta P_2,$$

where subscript 1 refers to the channel of the droplets and subscript 2 to the channel of the interface. With this expression, we calculate the variation in the pressure caused by the passage of a single droplet in the droplet channel. We found values in the range 8–50 Pascals (blue circles in Fig. 11), which have a very good agreement with the range obtained [(8–65) Pas, orange triangles in Fig. 11] by employing the droplet hydrodynamic resistance model proposed by Sajeesh et al. (2014) (for details, see Online Resource 2).
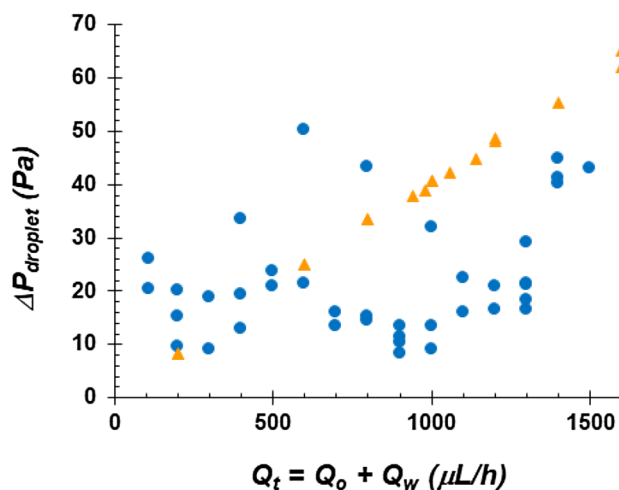

Fig. 11 Pressure drop generated by a single droplet in the droplet channel calculated from the interface movement (blue circles) or calculated with the droplet hydrodynamic resistance model proposed by Sajeesh et al. (2014) (orange triangles)

4 Conclusions

We designed a microfluidic device that generates a pulsatile pressure gradient without any electric or mechanical parts. As a proof of concept, it was employed to move periodically a fluid–fluid interface. Our device is based in a continuous stream of droplets that produces an oscillatory flow in an orthogonal channel. As the interface frequency matches precisely and with a dominant mode the frequency of the droplets, it can be easily fine-tuned by changing the flow rate of water and oil used to form the droplets. Besides, there are a vast number of variables that can be exploited to modify the pressure drop exerted by each passing droplet: droplet length and width, viscosity ratio between continuous and dispersed phases, droplet velocity, interfacial tension and even the presence of other droplets (Vanapalli et al. 2009; Sajeesh et al. 2014; Jakiela 2016). This richness in conditions could be harnessed to expand the possibilities of controlling a pulsatile flow with increased sensitivity. Additionally, the interface velocity data were used to estimate the pressure drop (8–50 Pa) caused by a single moving droplet in a rectangular channel solely with image analysis of the micrographs. Reduction of the sources of noise (e.g., using pressure pumps or soft elastomeric tubing for off-chip connections as in Kalantarifard et al. 2018) could in the future give more detailed information about the pressure of the continuous phase between droplets or at different parts of long droplets.

The construction of the single-layer-PDMS device used in this work is straightforward and its operation needs only two syringe or pressure pumps. Compared to other simple systems that use only syringe pumps to impose oscillatory movements, the frequency range of our device is at least 30- to 300-fold higher (3–34 Hz) than the syringe pumps that normally switch flow direction slowly (0.1–1 Hz) (Jo et al. 2009; Lestari et al. 2016; Alizadehgiashi et al. 2018). However, the oscillatory amplitude and pressure exerted by a syringe pump in a channel could be very high (several centimeters and 10^5–10^6 Pa) giving typical flow velocities from 10^2 to 10^5 μm/s (Jo et al. 2009; Lestari et al. 2016; Alizadehgiashi et al. 2018). In contrast, the amplitudes and flow velocities exerted by our device are very modest (2–12 μm and 100–1200 μm/s), but comparable to those obtained with piezoelectric actuated devices (5–20 μm; 10^3–10^5 μm/s) (Xie et al. 2015; Vázquez-Vergara et al. 2017). Based on these characteristics, the operating principle of our device could be used for mixing two or more fluids traveling in laminar flow by intersecting them with a perpendicular oscillating flow (Tabeling et al. 2004). Another possible application might be the extraction of organic compounds using the proposed pulsatile movement (Xie et al. 2015). Also, as the oscillatory driving force of our microfluidic device is only controlled by hydrodynamic elements, it could be coupled to other functional microfluidic circuits that work under the same principle. For instance, to fluidic capacitors (Leslie et al. 2009), which exert flow control in fluidic networks in accordance with the oscillating frequency at which they are excited.

5 Materials and methods

5.1 Fabrication of microfluidic devices

The microfluidic devices were built in PDMS by soft lithography (McDonald et al. 2000). A mould of SU-8 resist was fabricated and covered with PDMS base (Sylgard 184 silicone elastomer kit; Dow Corning Corp.) mixed with curing agent to a final concentration of 9% (w/w). After several hours of cross-linking at 65 °C, the PDMS was peeled off and the input and output ports were punched. The structured side of the PDMS was bonded against another flat slab of PDMS (0.9 cm thick) by oxygen plasma. The PDMS devices were incubated at least 48 h at 65 °C to ensure hydrophobicity after sealing. The flow-focusing geometry and the droplet transport channel had a rectangular geometry of 175 μm width and 83 μm height. The perpendicular channel for the oil-immiscible fluid had 73 μm width and 83 μm height.

5.2 Fluids

Pure deionized water (Millipore, density $\rho = 998$ kg m^{-3} and dynamic viscosity $\eta = 0.933$ mPa s at 23 °C) and mineral oil (Reactivos y Productos, Mexico, density $\rho = 850$ kg m^{-3} and dynamic viscosity $\eta = 56$ mPa s at 23 °C) containing 1.8% w/w of Span 80 (Sigma-Aldrich) were used for droplet production. The interfacial tension γ of these two liquids is 3.1 mN/m (Zhou et al. 2013). The ratio of water flow rate (Q_w) and oil flow rate (Q_o) was kept constant through all experiments and was equal to one ($Q_o/Q_w = 1$). The fluids for droplet formation were pumped into the device using syringe pumps (NE-1002X, New Era) and PTFE tubing (0.56 mm ID). The oil-immiscible fluid in the perpendicular channel was pure deionized water and was placed in an open syringe (atmospheric pressure) and introduced into the microfluidic device by gravity using rigid PTFE tubing (0.56 mm ID). A millimetric scale was used to determine the height of the column to calculate the hydrostatic pressure. The column height was adjusted such as the liquid–liquid interface lain between 360 and 1320 μm from the T-junction.

5.3 Imaging and data acquisition

An inverted microscope (DM IL LED, Leica) with a 10× or 20× objective (Leica) was coupled to a high-speed camera (Phantom Miro M110, Vision Research) and used to acquire high-speed videos at the T-junction of the microfluidic device. At this place, the passing droplets and the moving interface could be simultaneously captured. An analysis of the droplet channel allowed us to measure the droplet width, length, distance between droplets and the number of droplets per unit time from which we obtain the droplet frequency. The images of the pulsating interface were evaluated with a video-analysis software (Brown 2016) to obtain its position as a function of time. By comparing frame by frame the motion of the interface and the passing of droplets near the T-junction, we concluded that each passing droplet generates exactly one cycle of oscillation of the interface.

Author contributions ECP conceptualized the project. PAB performed the investigation. AT carried out the data curation and formal analysis. ECP and LFO did the funding acquisition and supervised the investigation. AT, ECP and LFO wrote the original draft, performed review and edited the final manuscript.

Compliance with ethical standards

Conflict of interest The authors declare that they have no conflict of interest.

Data availability The datasets generated during and/or analyzed during the current study are available from the corresponding author on reasonable request.

References

Abolhasani M, Jensen KF (2016) Oscillatory multiphase flow strategy for chemistry and biology. Lab Chip 16:2775–2784. https://doi.org/10.1039/c6lc00728g

Alizadehgiashi M, Khabibullin A, Li Y et al (2018) Shear-induced alignment of anisotropic nanoparticles in a single-droplet oscillatory microfluidic platform. Langmuir 34:322–330. https://doi.org/10.1021/acs.langmuir.7b03648

Baroud CN, Gallaire F, Dangla R (2010) Dynamics of microfluidic droplets. Lab Chip 10:2032. https://doi.org/10.1039/c001191f

Bengtsson K, Christoffersson J, Mandenius C-F, Robinson ND (2018) A clip-on electroosmotic pump for oscillating flow in microfluidic cell culture devices. Microfluid Nanofluidics 22:27. https://doi.org/10.1007/s10404-018-2046-4

Bordbar A, Taassob A, Zarnaghsh A, Kamali R (2018) Slug flow in microchannels: numerical simulation and applications. J Ind Eng Chem 62:26–39. https://doi.org/10.1016/j.jiec.2018.01.021

Brown D (2016) Tracker Video Analysis and Modeling Tool (Version 4.94). http://physlets.org/tracker/

Bruus H (2008) Theoretical Microfluidics. Oxford University Press Inc., New York

Chen H, Meng Q, Li J (2015) Thin lubrication film around moving bubbles measured in square microchannels. Appl Phys Lett 107:141608. https://doi.org/10.1063/1.4933105

Cheung P, Toda-Peters K, Shen AQ (2012) In situ pressure measurement within deformable rectangular polydimethylsiloxane microfluidic devices. Biomicrofluidics 6:026501. https://doi.org/10.1063/1.4720394

Duncan PN, Nguyen TV, Hui EE (2013) Pneumatic oscillator circuits for timing and control of integrated microfluidics. Proc Natl Acad Sci 110:18104–18109. https://doi.org/10.1073/pnas.1310254110

Garstecki P, Fuerstman MJ, Stone HA, Whitesides GM (2006) Formation of droplets and bubbles in a microfluidic T-junction—scaling and mechanism of break-up. Lab Chip 6:437–446. https://doi.org/10.1039/b510841a

Jakiela S (2016) Measurement of the hydrodynamic resistance of microdroplets. Lab Chip 16:3695–3699. https://doi.org/10.1039/c6lc00854b

Jo K, Chen Y-L, de Pablo JJ, Schwartz DC (2009) Elongation and migration of single DNA molecules in microchannels using oscillatory shear flows. Lab Chip 9:2348–2355. https://doi.org/10.1039/b000000x/Jo

Jose BM, Cubaud T (2014) Formation and dynamics of partially wetting droplets in square microchannels. RSC Adv 4:14962–14970. https://doi.org/10.1039/C4RA00654B

Kalantarifard A, Alizadeh Haghighi E, Elbuken C (2018) Damping hydrodynamic fluctuations in microfluidic systems. Chem Eng Sci 178:238–247. https://doi.org/10.1016/j.ces.2017.12.045

Kang C, Roh C, Overfelt RA (2014) RSC advances pressure-driven deformation with soft polydimethylsiloxane (PDMS) by a regular syringe pump: challenge to the classical fluid dynamics by comparison of experimental and theoretical results. RSC Adv 4:3102–3112. https://doi.org/10.1039/c3ra46708b

Khoshmanesh K, Almansouri A, Alblloushi H et al (2015) A multifunctional bubble-based microfluidic system. Sci Rep 5:9942. https://doi.org/10.1038/srep09942

Kim S-J, Yokokawa R, Cai Lesher-Perez S, Takayama S (2015) Multiple independent autonomous hydraulic oscillators driven by a common gravity head. Nat Commun 6:7301. https://doi.org/10.1038/ncomms8301

Kim G, Van Dang B, Kim S-J (2018) Stepwise waveform generator for autonomous microfluidic control. Sensors Actuators B Chem 266:614–619. https://doi.org/10.1016/j.snb.2018.03.160

Ładosz A, von Rohr PR (2018) Pressure drop of two-phase liquid-liquid slug flow in square microchannels. Chem Eng Sci 191:398–409. https://doi.org/10.1016/j.ces.2018.06.057

Leslie DC, Easley CJ, Seker E et al (2009) Frequency-specific flow control in microfluidic circuits with passive elastomeric features. Nat Phys 5:231–235. https://doi.org/10.1038/nphys1196

Lestari G, Salari A, Abolhasani M, Kumacheva E (2016) A microfluidic study of liquid-liquid extraction mediated by carbon dioxide. Lab Chip 16:2710–2718. https://doi.org/10.1039/c6lc00597g

Lignel S, Salsac A-V, Drelich A et al (2017) Water-in-oil droplet formation in a flow-focusing microsystem using pressure- and flow rate-driven pumps. Colloids Surfaces A Physicochem Eng Asp 531:164–172. https://doi.org/10.1016/j.colsurfa.2017.07.065

McDonald JC, Duffy DC, Anderson JR et al (2000) Fabrication of microfluidic systems in poly(dimethylsiloxane). Electrophoresis 21:27–40

Mosadegh B, Kuo C-H, Tung Y-C et al (2010) Integrated elastomeric components for autonomous regulation of sequential and oscillatory flow switching in microfluidic devices. Nat Phys 6:433–437. https://doi.org/10.1038/nphys1637

Qu J, Wu H, Cheng P et al (2017) Recent advances in MEMS-based micro heat pipes. Int J Heat Mass Transf 110:294–313. https://doi.org/10.1016/j.ijheatmasstransfer.2017.03.034

Raj A, Sen AK (2016) Flow-induced deformation of compliant microchannels and its effect on pressure–flow characteristics. Microfluid Nanofluidics 20:31. https://doi.org/10.1007/s10404-016-1702-9

Sajeesh P, Doble M, Sen AK (2014) Hydrodynamic resistance and mobility of deformable objects in microfluidic channels. Biomicrofluidics 8:054112. https://doi.org/10.1063/1.4897332

Tabeling P, Chabert M, Dodge A et al (2004) Chaotic mixing in cross-channel micromixers. Philos Trans R Soc A Math Phys Eng Sci 362:987–1000. https://doi.org/10.1098/rsta.2003.1358

Vanapalli SA, Banpurkar AG, Van Den Ende D et al (2009) Hydrodynamic resistance of single confined moving drops in rectangular microchannels. Lab Chip 9:982–990. https://doi.org/10.1039/b815002h

Vázquez-Vergara P, Torres Rojas AM, Guevara-Pantoja PE et al (2017) Microfluidic flow spectrometer. J Micromech Microeng 27:077001. https://doi.org/10.1088/1361-6439/aa71c2

Wang B, Xu JL, Zhang W, Li YX (2011) A new bubble-driven pulse pressure actuator for micromixing enhancement. Sensors Actuators A Phys 169:194–205. https://doi.org/10.1016/j.sna.2011.05.017

Wang X, Zhao D, Phan DTT et al (2018) A hydrostatic pressure-driven passive micropump enhanced with siphon-based autofill function. Lab Chip 18:2167–2177. https://doi.org/10.1039/c8lc00236c

Xie Y, Chindam C, Nama N et al (2015) Exploring bubble oscillation and mass transfer enhancement in acoustic-assisted liquid-liquid extraction with a microfluidic device. Sci Rep 5:12572. https://doi.org/10.1038/srep12572

Zhang Q, Zhang M, Djeghlaf L et al (2017) Logic digital fluidic in miniaturized functional devices: perspective to the next generation of microfluidic lab-on-chips. Electrophoresis 38:953–976. https://doi.org/10.1002/elps.201600429

Zhou H, Yao Y, Chen Q et al (2013) A facile microfluidic strategy for measuring interfacial tension. Appl Phys Lett 103:234102. https://doi.org/10.1063/1.4838616